

Experimental study of the coherent vorticity in slightly under-expanded supersonic screeching jets

International Journal of Aeroacoustics

2019, Vol. 18(2–3) 207–230

© The Author(s) 2019

Article reuse guidelines:

sagepub.com/journals-permissions

DOI: 10.1177/1475472X19834530

journals.sagepub.com/home/jae



Bertrand Mercier¹ , Thomas Castelain² and Christophe Bailly¹

Abstract

The noise generation mechanism of screech tone by shock leakage in underexpanded round jets is experimentally investigated by means of phase-averaged velocity fields. Two jet flows at Mach numbers 1.10 and 1.15 are measured by a particle image velocimetry apparatus simultaneously with their near acoustic fields and sorted according to their phase with respect to a screech period. The coherent vorticity fields are then computed and analyzed. They depict two distinct regions of high level of vorticity fluctuations. Thanks to the knowledge about shock leakage gathered in previous studies, the role of both regions in the acoustic generation process is identified and a region of the flow is recognized as suitable for emitting acoustic waves. Phase-averaged schlieren visualizations are also computed and used to determine the motion of the first five shocks over a screech period. For both jets, the peak shock motion is found at the fourth shock tip. This shock is also located in the region recognized as favorable for the shock leakage to be observed.

Keywords

Underexpanded jet, screech, experimental study, particle image velocimetry, schlieren

Date received: 8 February 2019; accepted: 8 February 2019

Introduction

Screech noise is a tonal component produced by imperfectly expanded supersonic jets. It was first identified by Powell¹ as a phenomenon emerging from an acoustic feedback

¹Univ Lyon, Ecole Centrale de Lyon and LMFA UMR CNRS 5509, Ecully, France

²Univ Lyon, Université Lyon 1 and LMFA UMR CNRS 5509, Ecully, France

Corresponding author:

Bertrand Mercier, Laboratoire de Mécanique des Fluides et Acoustique, Ecole Centrale de Lyon, LMFA UMR CNRS 5509, Ecully, France.

Email: B.H.Mercier@tudelft.nl

mechanism. From this pioneering work, it has been accepted that the feedback loop can be split into hydrodynamic structures convected in the jet mixing layer, and acoustic waves propagating upstream that initiate the generation of new structures when reaching the nozzle. Acoustic waves are produced by the interaction between the hydrodynamic structure and the periodic shock-cell pattern. The principle of this loop is now widely accepted in aeroacoustics, but the complex mechanisms causing the acoustic radiation and the acoustic receptivity of the mixing layer remain an ongoing research topic. Fairly accurate models^{2–5} indeed allow for screech frequency prediction, but the understanding of the process in terms of gain is necessary for predicting screech intensity. The receptivity has been indirectly investigated by modifying the acoustic field through the use of reflectors^{6–9} and absorbent panels^{10,11} near the nozzle, and the flow itself with different shapes of nozzle lip,^{12–15} but has not yet been modeled. Several theoretical approaches have nevertheless been developed over time. Tam's theory^{16,17} rests upon the linear interaction between the screech instability waves, and the periodic shock-cell pattern that produces an upstream propagating wave at screech frequency which travels at the speed of sound. A second theory^{18–21} relies on the acoustic emission by shock leakage across the mixing layer, but suffers from a lack of quantitative data to be fully established. The aim of the present work is to provide such data complementary with those proposed by Edgington-Mitchell et al.²² for the helical mode. In particular, the study focuses on the experimental characterization of the coherent vorticity field that plays a critical role in shock leakage.

Screech displays various modes associated with different frequency stages that depend upon the nozzle pressure ratio (NPR). These modes are axisymmetric, flapping, or helical and described in Ramanib's review²³ for round jets. The present study will focus on under-expanded jets exhausted from a convergent nozzle at low supersonic Mach number, for which only the axisymmetric modes called A1 and A2 are observed. For two jets, the velocity and vorticity fields coherent with the screech tone are extracted from particle image velocimetry (PIV) measurements of the planar velocity field, thanks to phase averaging post-processing. A mechanism for screech radiation based on the shock leakage is proposed, and a region of possible upstream propagating acoustic radiation is identified. These results are finally put together with the shock dynamics determined from phase-averaged schlieren measurements on the same jets to provide a complete picture of screech.

Experimental setup

The present experiments were conducted in the 10 m × 8 m × 8 m anechoic wind tunnel of the Center for Acoustic at École Centrale de Lyon. The wind tunnel is equipped with a high pressure compressor and a high flow rate centrifugal fan. In the present experiment, the high pressure supply is connected to a convergent nozzle²⁴ of exit diameter $D = 38$ mm. A secondary convergent nozzle coaxial to the primary one of diameter 236 mm is also used and fed by the fan. The exit plane of this secondary nozzle is located 135 mm upstream of the exit plane of the primary one. For this study, the NPR of the jets generated by the primary nozzle are $\text{NPR} = 2.14$ and $\text{NPR} = 2.27$ that correspond to fully expanded jet exhausted at a Mach number $M_j = 1.10$ and $M_j = 1.15$ and to Reynolds numbers of $Re_D = 8.5 \times 10^5$ and $Re_D = 8.9 \times 10^5$, respectively. The NPR is monitored during experiments and was found to remain constant within $\pm 0.3\%$. The secondary flow is only used for flow seeding purpose during PIV measurement, with an exit velocity of approximately 10 m/s.

PIV was applied to measure planar velocity fields of the two jets. Illumination is provided by a Litron Bernoulli 200–15 laser at 532 nm wavelength with 2×200 mJ pulse energy. The laser sheet crosses the jet through its axis and covers a usable field of $3D$ in the axial direction, and $\pm 1.5D$ around the jet axis in the radial direction. Particle images are acquired by a PCO.edge 5.5 camera mounted perpendicular to the laser sheet at a distance of 1 m. It is equipped with a 135 mm lens and an additional 20 mm extension ring. The images contain 2560×2160 pixels covering a field centered on the jet axis of axial and radial extents $2.9D$ (110 mm) and $2.4D$ (90 mm). The images are separated by $2 \mu\text{s}$ at a repetition rate of 15 Hz. For each studied case, data are made of three set of acquisitions shifted by $2.5D$ that results in a field of physical size $7.4D \times 2.4D$. The primary jet is seeded by an oil droplet generator, and the secondary flow is seeded with smoke. The relaxation time of the particles has been recognized as satisfactory in André et al.²⁵ for this configuration. The post-processing is performed by LaVision DaVis 7 with initial interrogation windows of 32×32 ($0.04D \times 0.04D$) pixels decreasing to 8×8 ($0.01D \times 0.01D$) with 50% overlap and two passes per window size.

A conventional Z-type schlieren apparatus was also used to visualize the flow. It consists of two $f/8$ parabolic mirrors of diameter 200 mm separated by 2.5 m, a high-power Cree XP-L LED as light source, and a knife edge set perpendicular to the jet axis. Images are recorded at a sampling rate of 18,000 frames per second by a Phantom V12 CMOS camera equipped with a Sigma 120–400 mm $f/4$ –5.6 lens. The exposure time of the images is $4 \mu\text{s}$, which is approximately equal to 1/40th of the screech period for both jets.

Phase averaging

Particle image velocimetry

Phase-averaged flow description consists in determining the evolution of an arbitrary quantity with its phase with respect to a given periodic phenomenon. A first method consists in triggering the acquisition of data from a reference signal. This method has for instance been used in the investigation of the screech phenomenon by Westley and Wolley,²⁶ Panda²⁷ or Alkislar et al.²⁸ from schlieren visualization, near field pressure, density measurements, or PIV measurements. The quality of the phase reference, however, rests upon the reference signal that must be cleaned from any noise contamination. For the screech tone, the reference signal can be the acoustic pressure measured in the upstream direction of the jet which is already a well demarcated peak in the spectrum. This is illustrated in Figure 1 by an example of pressure spectra measured in the nearfield and farfield of the two jets considered in this study. Nevertheless, even though in the nearfield the screech tone emerge by 26 dB for $M_j = 1.10$, and by 34 dB for $M_j = 1.15$, the broadband noise contribution to the signal cannot be neglected. Therefore, this signal is in general bandpass filtered to increase the phase trigger precision. The bandwidth of the filter must be as narrow and as steep as possible, which requires the use of a high-order filter. Such a filter is associated with a strong frequency dependent phase lag. As a consequence, a shift of frequency during measurement results in a shift of the phase of the reference signal. PIV measurements involve long records during which a slight screech frequency drift is likely to occur, due for instance to a possible small change in flow exhausting conditions. In order to avoid this difficulty, it is here chosen to record simultaneously the acoustic pressure near the nozzle, and the trigger signal of the laser Q-switch, as performed by Henderson et al.²⁹ for impinging jets. The phase in the screech loop at which the Q-switch is triggered is random and can be

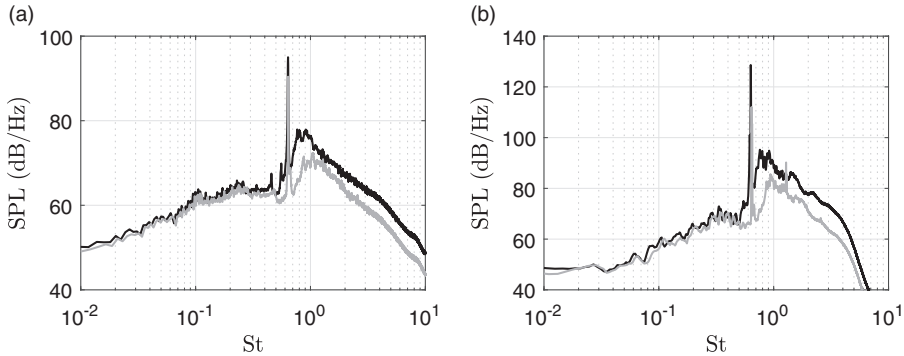


Figure 1. (a) Acoustic spectrum at 140° with respect to the jet axis and at a distance of $50D$. (b) Acoustic spectrum measured at 110° and $5.5D$. — $M_j = 1.15$, — $M_j = 1.10$.

determined from the recording. Similarly to the first method, the reference signal is obtained from the acoustic pressure signal through a bandpass filtering. However, the signal is numerically filtered during the post-processing. It is therefore easier to design a high-order filter which can be applied in a zero phase lag way, ensuring no dependency of the reference with regard to the measured screech frequency. Only an insignificant error remains from the associated drift in the acoustic wavelength since both the acoustic source and the microphone are fixed. The filter used is a 10th-order IRR bandpass filter centered on the screech frequency with a bandwidth equal to 3% of the screech frequency. The filtered reference pressure signal p_{ref} is an almost perfect sinewave from which the phase reference Φ_{ref} is extracted as follows

$$\Phi_{ref} = \arctan\left(\frac{\mathcal{H}(p_{ref})}{p_{ref}}\right) \quad (1)$$

where $\mathcal{H}(p_{ref})$ is the Hilbert transform of p_{ref} . The phase resolution is determined by the sampling frequency of the acoustic signal, namely 1 MHz in this study, corresponding to a resolution as small as 4×10^{-2} rad for the phase. The number of bins to divide the screech period is arbitrarily set to 18. All Q-switch events, namely velocity fields, are sorted in those bins with respect to their phase in the reference signal, and finally, all fields in a given bin are averaged resulting in velocity fields cleaned from most of the random turbulence contribution. All the phase-averaged quantities \tilde{q} of a given variable q results in

$$\tilde{q} = \bar{q} + q^{sc}(\Phi_k) \quad (2)$$

where \bar{q} is the time-averaged value of $q = \bar{q} + q'$, q^{sc} is the screech associated, or coherent component, and $\Phi_k = 2\pi i/18$ for $i = 0, \dots, 17$. In total, 3500 images were recorded per case to ensure a good convergence for the phase averaging.

Schlieren

Schlieren visualizations do not require an external signal to perform the phase averaging since the chosen field of view already contains some region of the flow at rest where the

screech is mostly the only contribution. The gray-level signal taken at the point $z = 0.7D$ and $y = 1.0D$ serves as the reference. The sampling frequency of the record is only approximately three times the screech frequency which is insufficient for estimating the phase with a satisfying precision by means of the Hilbert transform method. The phase Φ in the screech cycle is therefore determined by another mean. For each image, only a short sequence of the reference signal is considered. It starts three images before the one whose phase must be determined, and finishes three images after, making a seven-point long signal. This short signal is fitted by the function

$$A \sin(2\pi f_s t_k - \Phi) + C, \quad t_k = (-3, -2, \dots, 3)/f_{acq} \quad (3)$$

from which A , C , and Φ have to be determined, and f_s is the screech frequency obtained from the schlieren film. When the phase is known for all images, the same sorting and averaging process is applied as with PIV data.

Results

Time-averaged flow features

An overview of the flow structure is first offered through the time-averaged velocity, the fluctuating velocity, and the spanwise vorticity component $\omega = \partial u / \partial y - \partial v / \partial x$. These fields are presented in Figure 2, remembering that $q = \bar{q} + q'$ with $q_{rms}' = q'^2^{1/2}$. The mean velocity fields are marked by the shock-cell pattern that characterizes the structure of non-ideally expanded jets. The end of the first five shock cells where the compression waves are reflected into expansion waves is indicated by a dashed line. This reflection occurs at the sonic line³⁰ represented by a solid line, whose position is determined by estimating the local static temperature T following the Crocco-Busemann relation³¹

$$\frac{T}{T_j} = \frac{T_{amb}}{T_j} + \left(1 + \frac{(\gamma - 1)}{2} M_j^2 - \frac{T_{amb}}{T_j} \right) \frac{u}{U_j} - \frac{(\gamma - 1)}{2} \frac{u^2}{a_j^2} \quad (4)$$

where T_{amb} is the ambient static temperature, $M_j = U_j/a_j$ is the jet Mach number based on the velocity U_j and on the speed of sound $a_j = \sqrt{\gamma r T_j}$ with T_j the jet static temperature. The index j denotes the value of a quantity corresponding to the perfectly expanded jet. Among the other assumptions for its derivation, equation (4) holds for an isentropic flow and is thus used along the subsonic region frontier to determine the sonic line position. Nevertheless, the flow across the weak shocks contained in the supersonic jet plume is also expected to be isentropic, and conditions to use equation (4) might also be satisfied there. By examining the mean transverse velocity field in Figure 2, it may be observed that the location of the sonic line is found in good agreement with the position of the shock cell structure.

The axial velocity fluctuations reach a constant value close to $0.2U_j$ in the shear layer for $M_j = 1.15$ against $0.16U_j$ for $M_j = 1.10$. A similar trend is observed for the radial velocity fluctuations, as it may be better observed in Figure 3. These higher fluctuations must be linked to the higher acoustic pressure level at screech frequency, refer to Figure 1.

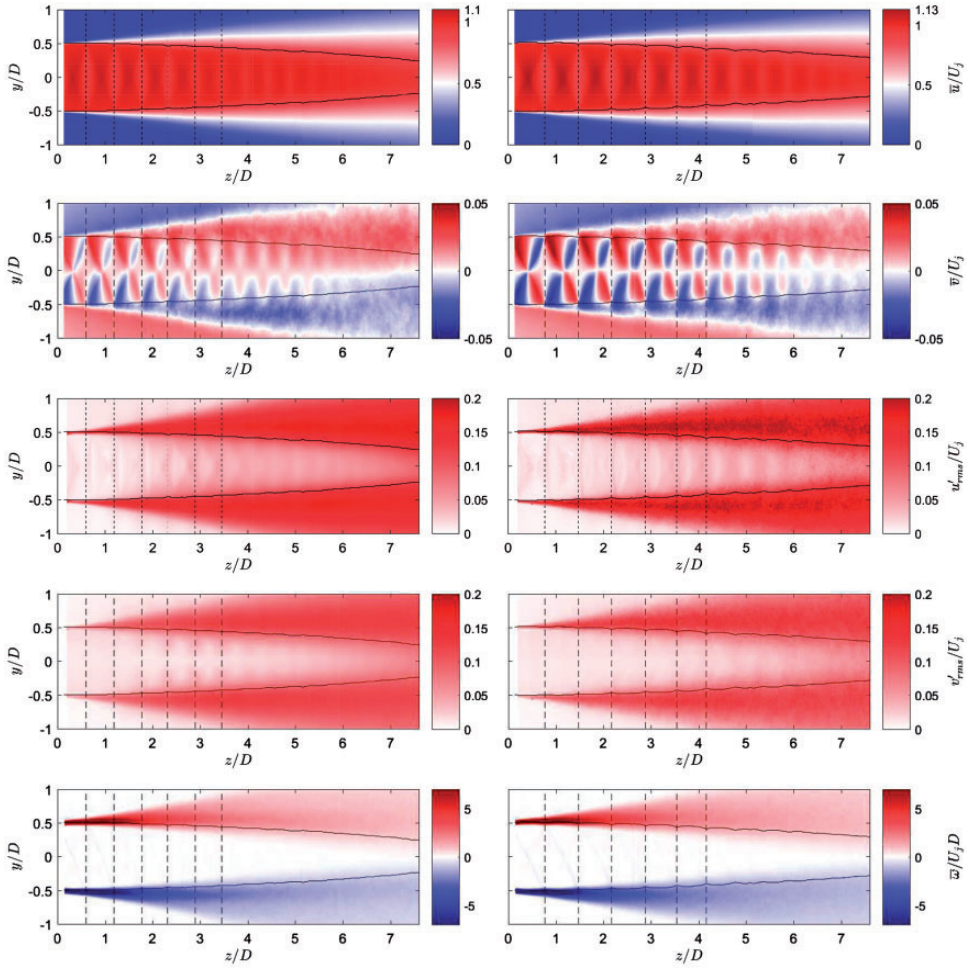


Figure 2. Contour of the mean and fluctuating velocity components and the mean vorticity for $M_j = 1.10$ (left) and $M_j = 1.15$ (right). The vertical dashed lines indicate the first five shock positions, and the solid line indicates the sonic line.

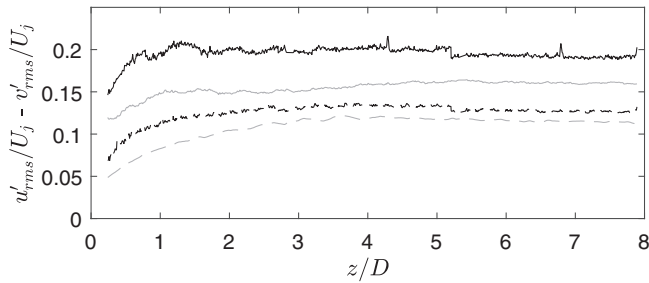


Figure 3. Evolution of the axial (—) and radial (- -) peak velocity fluctuations along the mixing layer. — $M_j = 1.15$, - - $M_j = 1.10$.

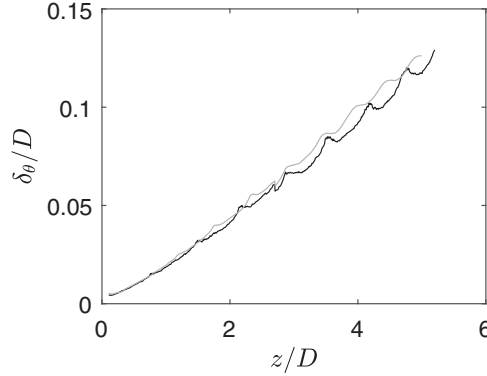


Figure 4. Evolution of the momentum thickness along the mixing layer. — $M_j = 1.15$, - - $M_j = 1.10$.

Krothapalli et al.³² have shown in their experimental study that fluctuations in the mixing layer of screeching rectangular jets increase with the screech amplitude. This is also observed in the PIV measurements by André et al.,³³ who used a notched nozzle to remove the screech component, and in the experiment results by Edgington-Mitchell et al.²² and Tan et al.³⁴ for similar Mach numbers. A turbulence intensity close to $0.16U_j$ is reported in the former study, while a turbulence intensity beyond $0.20U_j$ was found by the latter study. The time-averaged vorticity is also represented in Figure 2, and no significant difference between the two jets can be highlighted.

Both jets are forced by screech tone at a Strouhal number approximately equal to $St_D = 0.65$, which meets the range of frequencies causing instability waves amplification, and promoting turbulent mixing. The spatial evolution of the jet momentum thickness computed following the method proposed in André et al.,²⁵ is plotted in Figure 4. The spreading rate is found to be $d\delta_\theta/dz \simeq 0.046$, which is a higher value than for unforced jets.³⁵

Phase-averaged flow features

Coherent velocities

It has been observed in the previous section that the two jets have a similar structure, but they differ by their velocity fluctuation levels. The screech associated contribution (2) of the velocity fluctuations is now investigated independently from turbulent fluctuations. Figure 5 displays the coherent axial and radial velocity fluctuations, and the coherent vorticity. For all these quantities, the magnitude is found lower for the $M_j = 1.15$ jet than for the $M_j = 1.10$. It is not expected to observe a direct simple link between the coherent fluctuations, and the screech tone level. The latter is indeed determined by a complex generation mechanism; moreover, the screech forcing does not correspond to a classical configuration of excited flows.³⁶

A second general observation concerning the velocity fluctuations is the noticeable modulation of u_{rms}^{sc} and v_{rms}^{sc} by the shock cells, already described in the literature.^{22,37–40} Besides, u_{rms}^{sc} is found to be maximum inside a region bounded by the sonic line, to be minimum at the lip line, and to be weak in the low-speed region of the mixing layer. Conversely, v_{rms}^{sc} is maximum near the lip line and decreases beyond. These two features are the signature of a

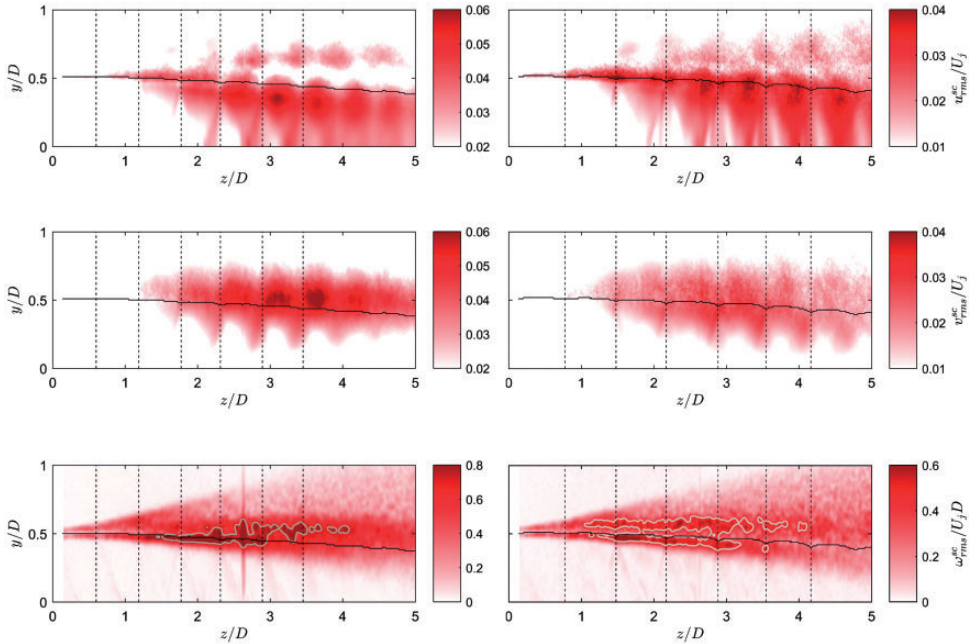


Figure 5. Statistics of the coherent component in the $M_j = 1.10$ (left) and the $M_j = 1.15$ (right) jets. Note the change in scale between the $M_j = 1.10$ and $M_j = 1.15$ jets. The vertical dashed lines indicate the first five shock positions and the solid line corresponds to the sonic line.

convected vortex of size close to the local mixing layer thickness. The tilting of the shock cells also produces coherent fluctuations in both directions that appear in the jet core. Additionally, the potential core is affected by coherent fluctuations induced by the passage of the large structures in the mixing layer. It should finally be noted that the modulation of u_{rms}^{sc} is not spatially synchronized in the inner and the outer mixing layer regions. Indeed, except for the first three shock cells of the $M_j = 1.15$ jet, in the supersonic region maximum levels of u_{rms}^{sc} occur barely in the middle of the shock cells with respect to the streamwise direction, whereas they are aligned with the shock tips in the low-speed region. This behavior is similar with the experimental observations by Ecker et al.³⁹ in a $M_j = 1.4$ overexpanded jet, or by Edgington-Mitchell et al.²² in a $M_j = 1.45$ jet, even though the maximum is found shifted toward the center of the shock cells in the present case in comparison with the two latter studies. This difference possibly arises from the difference in screech mode between these two studies in which helical mode is observed, whereas A1 and A2 modes of the present study are axisymmetric.

Coherent vorticity

Two regions in the shear layer where ω_{rms}^{sc} exhibits large values can be observed in the fluctuating vorticity map in Figure 5 (refer to white contours). They correspond either to high-velocity regions or lower velocity regions. For $M_j = 1.10$, the maximum of ω_{rms}^{sc} is first obtained in the high-velocity region for $z/D < 3$. In the same axial range, high values of ω_{rms}^{sc} are also visible as local maxima in the lower velocity region. For $z/D > 3$, values in the high-

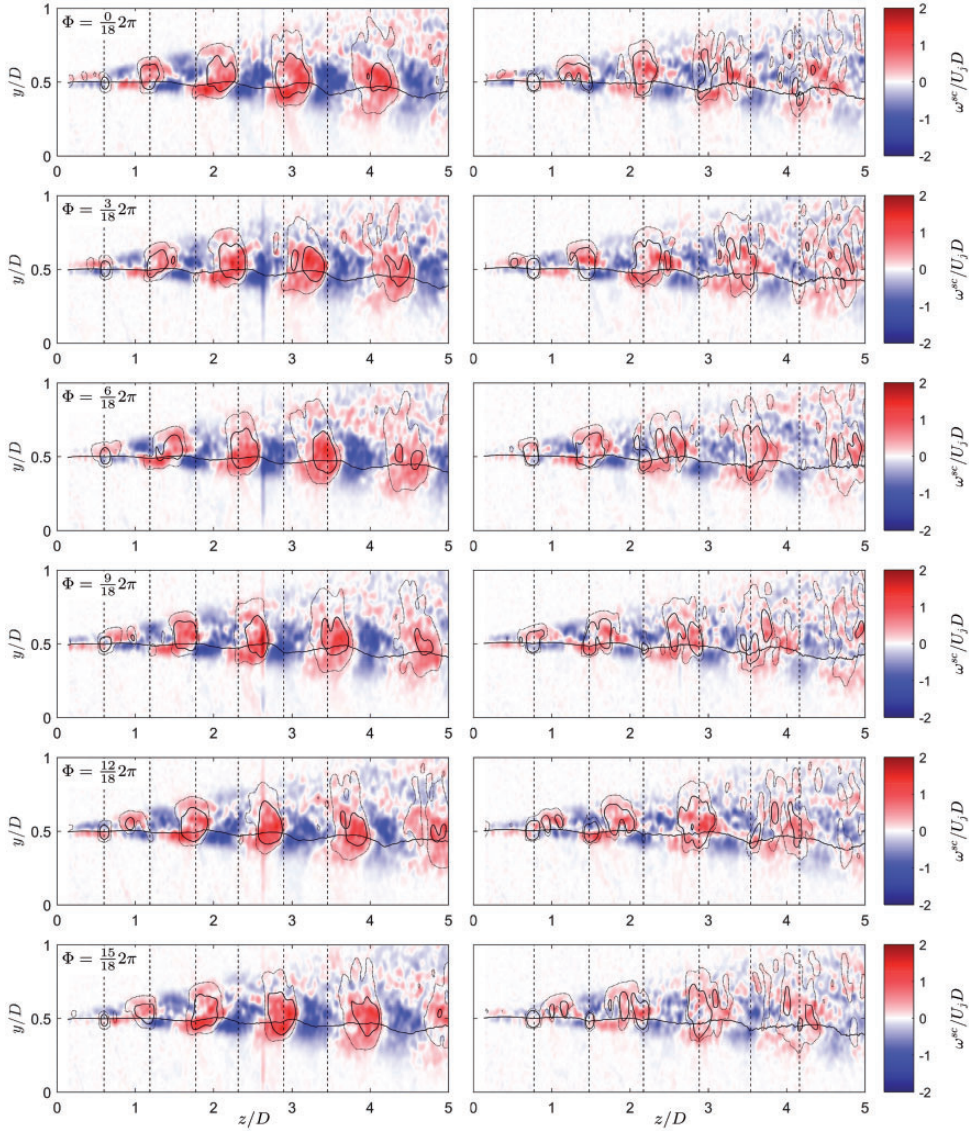


Figure 6. Snapshot of the coherent vorticity $\omega^{sc}(\Phi)$, for $M_j = 1.10$ (left) and $M_j = 1.15$ (right). The vertical dashed line indicates the first five shock positions, the solid line corresponds to $u = 0.85U_j$, and the isocontours are provided by the Q-criterion.

velocity region decrease, and the maximum is located in the lower velocity region. For $M_j = 1.15$, the two regions of local maximum for ω_{rms}^{sc} are again observed. The region in the low-speed side appears to extend further downstream than that in the high-speed side. The same pattern is also visible in recent results obtained by Edgington-Mitchell et al.⁴¹

The time evolution of the coherent vorticity ω^{sc} over of the screech period is shown in Figure 6. A low-pass Gaussian filter of standard deviation two grid points ($0.02D$) has been applied to the images in order to improve the readability. A well-organized pattern of

positive and negative vorticity spots can be seen. The positive vorticity here corresponds to vortex cores whereas the negative vorticity must be associated with saddle points since the mean flow is not included.

The line corresponding to $\bar{u} = 0.85U_j$, that is close to the sonic line, is also superimposed. Following the path of this line, the flow is deflected toward outside in region of high vorticity, and toward the core of the jet at the saddle points. This behavior can be observed with more details in the films provided in supplementary material for both jets. The time evolution of the high coherent vorticity $\omega^{sc}(\phi)$ spots is shown, in addition with the coherent velocity field ($u^{sc}(\phi)$, $v^{sc}(\phi)$), and with time-averaged axial velocity contours. In order to better identify the flow deflection, the line at which $\bar{u} = 0.85U_j$ is also plotted in green and the line at which $\bar{u} + u^{sc}(\phi) = 0.85U_j$ is plotted in blue.

Near the nozzle, the vorticity spots are in opposition of phase in the inner and the outer part of the mixing layer for both jets. Downstream, this phase shift tends to decrease with increasing z/D . The varying phase shift indicates a difference of phase velocity in the two regions of high vorticity fluctuations shown in Figure 5. The next paragraphs are dedicated to the analysis of these two regions.

A first analysis consists in comparing the Q-criterion and the vorticity field, as illustrated in Figure 6. The Q-criterion can only be calculated in the PIV plane, which yields

$$Q = (\Omega_{ij}\Omega_{ij} - S_{ij}S_{ij})/2 = -\frac{\partial u^{sc}}{\partial y} \frac{\partial v^{sc}}{\partial x} - \frac{1}{2} \left(\left(\frac{\partial u^{sc}}{\partial x} \right)^2 + \left(\frac{\partial v^{sc}}{\partial y} \right)^2 \right) \quad (5)$$

where Ω_{ij} and S_{ij} are the anti-symmetric and symmetric components of the velocity gradient tensor. The contour in solid line corresponds to a convenient Q-criterion value, and the dotted line corresponds to the contour of a tenth of that value. As well illustrated by the $M_j = 1.10$ jet between $z/D = 1$ and $z/D = 3$, the high level of vorticity in the supersonic region is not connected to the vorticity in the low speed region by contours of Q-criterion. The same feature is also observed in the $M_j = 1.15$ case, but the lower signal-to-noise ratio prevents from providing an unambiguous result. Beside, this observation is supported by the spatial distribution Q_{rms} of the rms fluctuation of the Q-criterion presented as a contour superimposed to the vorticity fluctuations in Figure 7. This figure also depicts phase contours that will be analyzed later. The relevant point to observe at this step is the symmetrical expansion of Q_{rms} around the high vorticity region located in the low speed side of the mixing layer, but that does not include the inner high vorticity region.

High values of Q-criterion indicate that the outer region of high vorticity is associated with the screech coherent structures. The second region of high vorticity appearing in inner side of the mixing layer is less immediate to interpret. To address this question, the analysis is focused on the flow features around vortices. At this stage, the phase-averaged results still contain too much noise for the maps to be unambiguously interpreted. Therefore, we propose a dedicated data treatment to provide smoother vorticity fields that consists in averaging the flow field around an arbitrary chosen vortex over different phases in the screech period. This processing is carried out by defining a rectangular window that contains the chosen vortex. For the first phase step the window is centered around the vortex. For the next phase step, a second window initially at the same position as the first one is considered. A 2D cross-correlation is then computed between the coherent vorticity field ω^{sc} in each window. The position of the maximum of correlation indicates the spatial shift to apply to

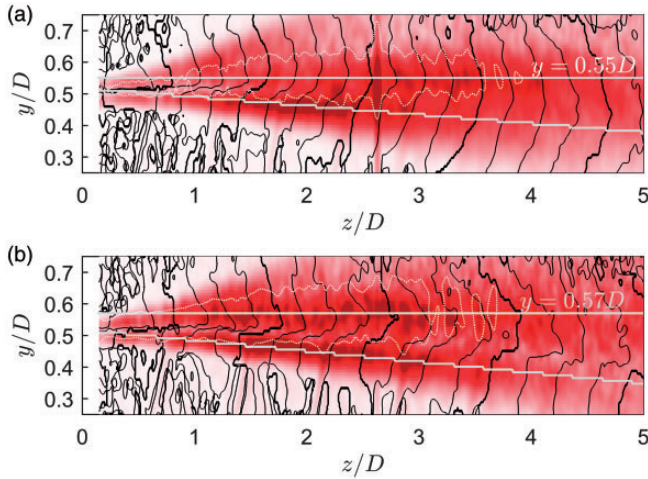


Figure 7. Contours of the phase $\Phi_{\omega^{sc}}$ every $\pi/2$ superimposed on ω_{rms}^{sc} . The dotted line is an isocontour of the Q-criterion fluctuations Q_{rms}^{sc} , and the white lines indicate the location of maximum ω_{rms}^{sc} . (a) $M_j = 1.10$ and (b) $M_j = 1.15$.

the second window to track the vortex. The process is repeated for the following phase steps by considering each time the window of the previous phase step as new reference. The result of the procedure is a set of flow fields, all containing the same vortex at different phase steps, and approximately at the same position in the window. This set of fields is averaged to obtain smoothed flow features denoted by $\langle \rangle$. The average resulting from this process is intrinsically biased by the spatial growth of the vortex, but this bias can be reduced by considering areas where the spatial evolution of the vortices pattern is weak. For both jets, vorticity maps displayed in Figure 6 show that this constraint is roughly respected between $z = 1.5D$ and $z = 3D$. The vortex tracking will therefore be restricted to this region. The bias introduced by the spatial growth of the vortex is estimated by performing averages across 6, 12, and 18 phase steps which corresponds to tracking the vortex over $1/2$, $3/4$, and 1 wavelength. The three results which are not presented here are similar, indicating that the effect of the spatial growth of the vortex can be neglected. Only the Q-criterion for $M_j = 1.15$ is found to strongly vary with the number of steps, and the initial position of the vortex. This lack of convergence can be linked together with the poor signal-to-noise ratio already observed in Figure 6. In the following, the first window is initially centered around $z = 1.5D$ and $y = 0.55D$, its axial and radial extents are $1.30D$ and $0.45D$.

The averaged axial and radial coherent velocities $\langle u^{sc} \rangle$ and $\langle v^{sc} \rangle$ are shown as vector plots superimposed on the averaged coherent vorticity $\langle \omega^{sc} \rangle$ in Figure 8. In addition to the coherent vorticity and velocities, the mixing layer is delimited from region of potential flow by gray lines at position where $\bar{\omega} + \langle \omega^{sc} \rangle = 0.1 \max(\bar{\omega} + \langle \omega^{sc} \rangle)$. For both jets, the maximum of $\bar{\omega} + \langle \omega^{sc} \rangle$ is close to $9 U_j/D_j$ and found at the center of the mixing layer in the upstream limit of the domain. Finally, contours of the Q-criterion are added for $M_j = 1.10$ only, $M_j = 1.15$ being omitted for clarity. Results shown in Figure 8 for $M_j = 1.10$ and $M_j = 1.15$ jets are very similar, and their main features are summarized in the sketch Figure 8(e). The flow consists of a vortex turning anti-clockwise, associated with a stagnation point upstream and downstream. The stagnation points are equivalent to

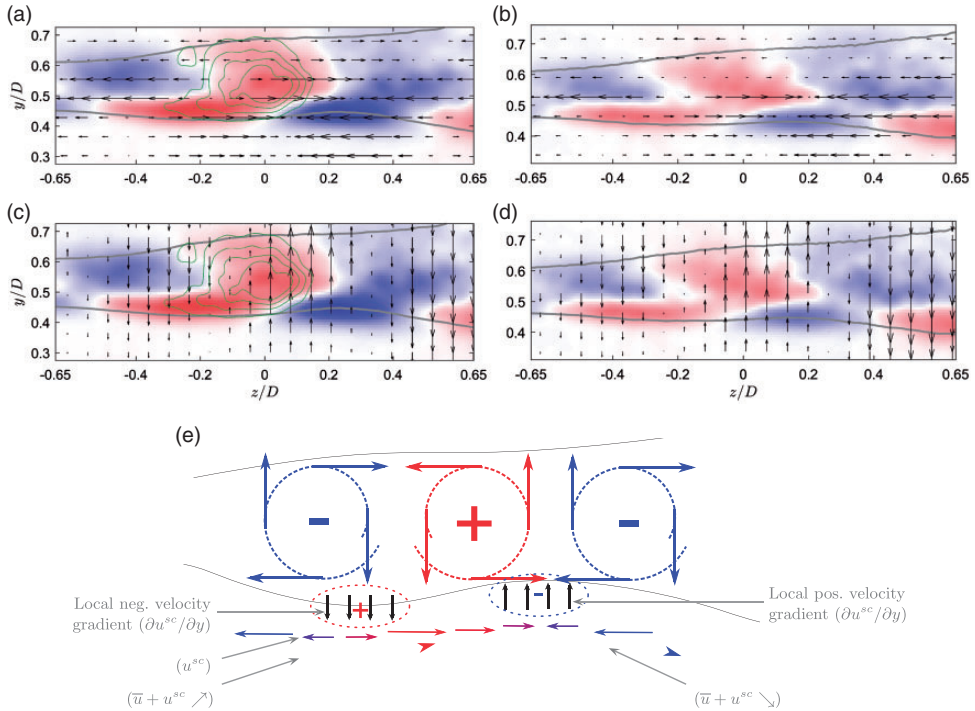


Figure 8. Spatially averaged vorticity around a vortex initially centered at $z/D = 1.5$. (a) and (b) $M_j = 1.10$. (c) and (d) $M_j = 1.15$. Arrows represent u^{sc} in their respective directions. Gray lines show the iso-vorticity contour $\bar{\omega} + \omega^{sc} = 0.1 \text{Max}(\bar{\omega} + \omega^{sc})$. Green lines show Q-criterion contours. (e) Diagram of the phenomenon.

vortices turning clockwise when the time-averaged vorticity is removed, as in the present case where only $\langle \omega^{sc} \rangle$ is considered. According to the contours of Q-criterion, and to the analysis proposed in the previous paragraphs, the vortex lays near the lip line at the center of the mixing layer. The vortex also deforms the boundary of the mixing layer. The convection velocity of this deformation is linked with the vortex convection velocity, and is close to $0.55U_j$.⁴⁰ The relative velocity between the flow in the potential core and the vortex in the mixing layer is thus around $0.45U_j$. Therefore, in the field of view displayed in Figure 8, positive curvature of the mixing layer boundary implies potential core flow acceleration, whereas negative curvature implies flow deceleration. When the average value of the velocity is removed, to only examine $\langle u^{sc} \rangle$, low speed and high speed, respectively, turn into positive and negative value for $\langle u^{sc} \rangle$. The combination of the vortex associated rotating flow in the mixing layer, and of its effect in the potential core, gives rise to two regions of strong axial velocity gradients in the radial direction near the inner boundary of the mixing layer, between the vortex core and the stagnation points. At the same positions, the radial velocity gradient is far weaker. Thus, gradients of the axial velocity component come in the form of vorticity in the inner part of the mixing layer, shifted by approximately a quarter of the screech hydrodynamic wavelength apart from the vortex core.

The phase shift between the two regions of high vorticity tends to decrease when z increases, as already mentioned above. In order to bring a quantitative analysis of this

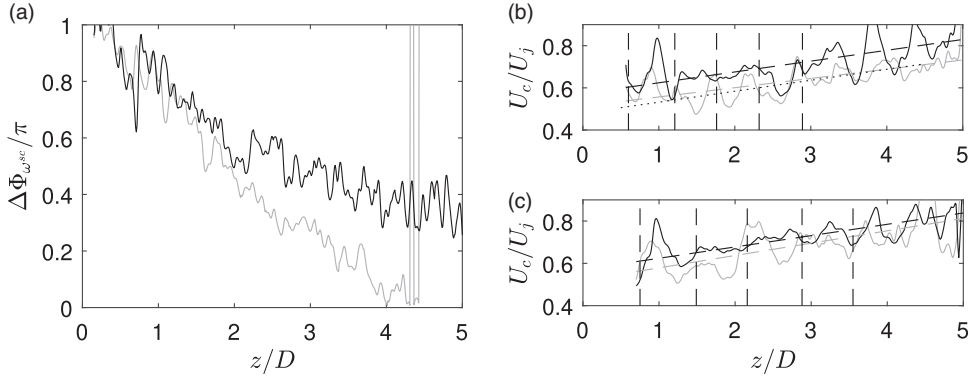


Figure 9. (a) Vorticity phase lag between the low- and high-speed regions for — $M_j = 1.10$, — $M_j = 1.15$, (b) $M_j = 1.10$, and (c) $M_j = 1.15$: convective velocity derived from the spatial phase evolution of the vorticity. — Low-speed side, — high-speed side, - - - fitted convective velocity, ··· schlieren data from Mercier et al.⁴⁰

phase shift evolution, and of the associated convection velocities, the phase $\Phi_{\omega^{sc}}$ is introduced as the argument of the second term of the Fourier series of the vorticity field at every position. The result is presented in Figure 7 as a contour superimposed on the coherent fluctuations of the vorticity through lines separated by $\pi/2$. For $M_j = 1.10$, there is a sharp jump of phase across the shear layer that tends to decrease in magnitude with increasing z/D . For $M_j = 1.15$, this same strong jump decreases from $z = 1.5D$ to $z = 3.5D$ and increases again downstream. The existence of such a sharp jump sustains that the evolution of the vorticity associated with the screech related structures in the mixing layer is in some ways independent from the vorticity spots laying in the supersonic region, which interact with the shock tips. Two lines that follow the maximum of the coherent vorticity fluctuations are defined for each case in Figure 7. The phase difference $\Delta\Phi_{\omega^{sc}}$ between the coherent vorticity along the two lines is shown in Figure 9(a). At the nozzle exit, the vorticity is in opposition of phase between the outer and the inner sides of the jet. The difference decreases monotonically with the axial distance indicating that the phase velocity of the vorticity is greater inside than outside the mixing layer. A convective velocity can be computed from the differentiation of the phase $d\Phi_{\omega^{sc}}(z)/dz$ through a linear regression of $\Phi_{\omega^{sc}}$ within the moving window $[z - L_{sc}/4, z + L_{sc}/4]$, where L_{sc} is the shock cell length. It yields

$$U_c(z) = \frac{2\pi f_s}{d\Phi_{\omega^{sc}}/dz} \quad (6)$$

Here, the filter width is chosen to keep the oscillation related to the shock-cell pattern as shown in Figure 9(b) and (c) with the resulting convective velocity. The ripple is more intense on the convective velocity measured in the low-speed region upstream of the third to the fourth shock tip. Beside, this ripple increases downstream of this region when the high-speed convective velocity is considered. Contrary to what is observed from density measurements by Rayleigh scattering in Panda³⁸ or by Schlieren measurements^{42,43} on the phase velocity that partially arises from the modulation of the hydrodynamic perturbation by the acoustic field, the present convective velocity calculated from the vorticity only

represents the hydrodynamic component. It is therefore demonstrated here that even in the supersonic region, where the mean flow undergoes compressions and expansions induced by the shock cells, the screech associated component remains unaffected when passing across the shock tips. The axial evolution of U_c is also provided in dashed line by a linear fit computed over the whole domain. The convective velocity increases with the axial distance as already observed in Mercier et al.,⁴⁰ with a similar rate in the low and high-speed regions. In addition, the linear trend of the phase velocity computed from schlieren data obtained by the authors in a previous study⁴⁰ is presented for the $M_j = 1.10$ jet in dotted line. This trend compares well with that obtained in the low speed side. The result for the $M_j = 1.15$ case derived from the previous schlieren visualizations is not presented since it is found strongly sensitive to the range of the derivative computation due to the high level of modulation of the hydrodynamic wave by the shock cells and the acoustic field.

In the end, two regions of high vorticity, which are related to two distinct phenomena induced by the screech feedback loop, are identified. The vorticity region that lays near the lip line in the low-speed side seems to correspond to the structures that dominate schlieren visualization and that are generally accounted for in the frequency prediction models. However, the coherent vorticity spots convected in the inner part of the mixing layer are more likely to interact directly with the shock tips.

A noise generation mechanism for screech

The interaction between the coherent structures and the shock-cell pattern that leads to the generation of the screech tone has already been investigated by many authors. The mechanisms identified in these studies can be divided into two main classes. The acoustic radiation would result from the shock leakage across the mixing layer,^{18–22,44–46} or the interaction between the instability wave and the shock-cell pattern would give rise to supersonic phase velocity perturbation, and therefore acoustic generation in the upstream direction.^{16,47,48} This second point of view brings up some issues if, for instance, the broadening of the wave number spectrum due to the growth and decay of the instability wave was considered and confronted to the narrowness of the screech tone observed in acoustic spectra. Similarly, the A2 mode does not meet the requirement of this theory in terms of wave numbers as pointed out in Mercier et al.⁴⁰ On the other hand, the mechanism by which the compression wave of the shock cell leaks across the mixing layer has been analyzed numerically and appears to be eligible for modeling the screech acoustic source. Suziki and Lele¹⁹ obtained satisfactory results by using a direct numerical simulation combined with geometrical acoustics on an idealized mixing layer. Berland et al.²⁰ directly observed the shock leakage phenomenon in their large eddy simulation of a planar jet.

In what follows, the hypothesis of screech tone radiation induced by a shock-leakage process is favored. From Suziki and Lele¹⁹ and Shariff and Manning,²¹ the shock leakage occurs in supersonic flows convecting vorticity spots, and in particular at the saddle points between two vortices as also shown in Berland et al.²⁰ The periodic passages of vorticity spots are directly associated with the coherent flow depicted in Figure 6. Two regions of high coherent vorticity have been identified above, near the lip line in the low speed region, and in the supersonic region. This second component directly interacts with the shock tips in a similar fashion as the idealized academic cases^{19,21} and would therefore be considered as responsible for the shock leakage. Suziki and Lele¹⁹ also demonstrated that the acoustic wave front is bended toward the upstream direction by passing across positive

vorticity spots. This second mechanism can be applied to the acoustic wave emerging from the shock leakage and that propagates into the high coherent vorticity region located near the lip line. This interaction would consequently increase the upstream directivity of the screech acoustic waves. As such a directivity is a necessary condition of the screech, this bending of wavefronts is supposed here to play a significant role in the screech phenomenon. In order to efficiently bend the wave front, the wave leaking at the saddle point of the inner high coherent vorticity region must meet a maximum of coherent vorticity near the lip line. A necessary phase shift between these two regions should therefore be around π if the shock leakage was omnidirectional, or to a smaller phase shift if an upstream directivity already resulted from the shock leakage as it is observed by Suzuki and Lele¹⁹ or Shariff and Manning.²¹

Based on this proposed mechanism, the feedback of the screech resonant loop rests upon high vorticity fluctuations ${}^i\omega_{rms}^{sc}$ in the inner region of the mixing layer defined by the inner white line in Figure 7, high vorticity fluctuations ${}^o\omega_{rms}^{sc}$ in the outer region, and a suitable phase shift $\Delta\Phi_{\omega^{sc}}$ given in Figure 9. In order to evaluate the local ability of the shear layer to sustain this mechanism, the following function C is introduced

$$C(z) = G_i({}^i\omega_{rms}^{sc})G_o({}^o\omega_{rms}^{sc})G_\phi(\Delta\Phi_{\omega^{sc}}) \quad (7)$$

where G_i , G_o , and G_ϕ are respectively three gain functions associated with the inner vorticity, the outer vorticity, and the phase shift between them. Gain functions are unknown, but in a first guess, one may simplify the shock leakage phenomenon by assigning a linear dependency to these functions. This is probably oversimplified, but more cases than available in this study would be required to identify these gain function. Following this principle, G_i can be $G_i = {}^i\omega_{rms}^{sc}$ and G_o be $G_o = {}^o\omega_{rms}^{sc}$. It seems reasonable to guess that G_ϕ should be maximum for $\Delta\Phi_{\omega^{sc}} \leq \pi$ and minimum for $\Delta\Phi_{\omega^{sc}} \simeq 0$. Since in the present case, $\Delta\Phi_{\omega^{sc}}$ varies between 0 and π , G_ϕ can simply be $G_\phi = \Delta\Phi_{\omega^{sc}}/\pi$.

The spatial evolution of the function $C(z)$ with these gains is shown in Figure 10. For both jets, C takes low values near the nozzle, then rises to a plateau, and finally decreases downstream of a given position. The plateau is comprised between the second and the fifth shock tip for $M_j = 1.10$ and between the first and the fourth for $M_j = 1.15$.

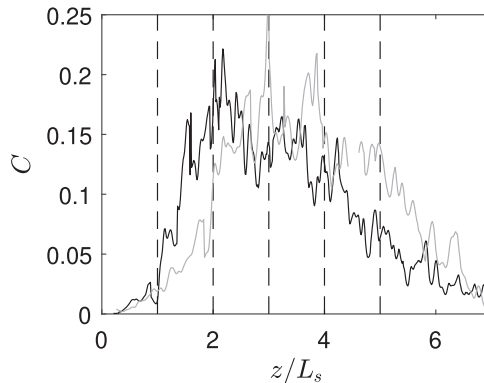


Figure 10. Spatial evolution of the function C (7) arbitrarily normalized. — $M_j = 1.10$, - - $M_j = 1.15$.

The range of maximum C is interpreted as the region where shock leakage is most likely to occur, and where the upstream directivity of the radiated acoustic waves should be maximum. The range found in this study is consistent with those determined in the literature for similar jets.^{4,5,18,40,41,49}

The results here presented, and obtained from phase-averaged vorticity fields, constitute a restricted sample of flows hosting the screech phenomenon. Despite that, original phenomena are pointed out, in particular the presence of a vorticity layer directly interacting with the shock tips, and convected at a velocity higher than that of the screech associated large structures. To the knowledge of the authors, this layer has not been considered in frequency prediction models even though they all rest upon the convection velocity of the hydrodynamic wave interacting with the shock-cells. It would be of great interest, regarding screech modeling purposes, to reproduce such results for more Mach numbers, and not only for axisymmetric modes. A larger database would allow to assess models fed by each of the two convective velocities and could bring up correlations between the screech amplitude and the vorticity field.

Shock motion

PIV measurements are well suited to study the vorticity and other flow features relying on the velocity field. However, a second essential contributor to the shock leakage is the shock cell structure of the jet. A very convenient method to observe shocks in flows is the schlieren visualization that emphasis density gradients. Furthermore, coupled with a high-speed camera, schlieren apparatuses allow to study the dynamic of the shocks. In the following, we take advantage of the periodic nature of the screech phenomenon to investigate the screech associated shock motion through phase averaging, following the method described in section *Phase averaging*.

The dynamic of the shock cells in a screeching jet was first studied by Panda⁵⁰ through schlieren visualizations and a dedicated instrumentation capable of detecting the passage of a shock into a light beam. The phase-averaged displacement of the first four shock tips of two jets exhibiting axisymmetric, and flapping screech modes were measured. The displacement was found to increase with the axial position of the shock tip. The complex and large motion of the core of the shock cells was also pointed out. More recently, the shock tip motion was measured by André et al.⁵¹ who showed a positive correlation between the amplitude of the shock motion and the screech sound level. These two studies provide accurate data on the shock motion for a given shock cell, but do not easily offer a global picture of the shock motions and of the vorticity field. There is nevertheless a clear interest, for modeling purpose, to determine the phase relationship between the shock motions and the coherent vorticity. Consequently, a shock-tracking procedure is developed and applied on the phase-averaged schlieren visualizations for both jets at $M_j = 1.10$ and $M_j = 1.15$. Outcomes of the shock tracking are phase-averaged shock tip positions that will be synchronized with the phase-averaged PIV results.

Shock tracking procedure

The shock tracking procedure is based on the phase-averaged schlieren visualizations. An example of schlieren results at six phases over a screech period are presented for the $M_j = 1.15$ jet in Figure 11. This figure also aims at describing the tracking procedure.

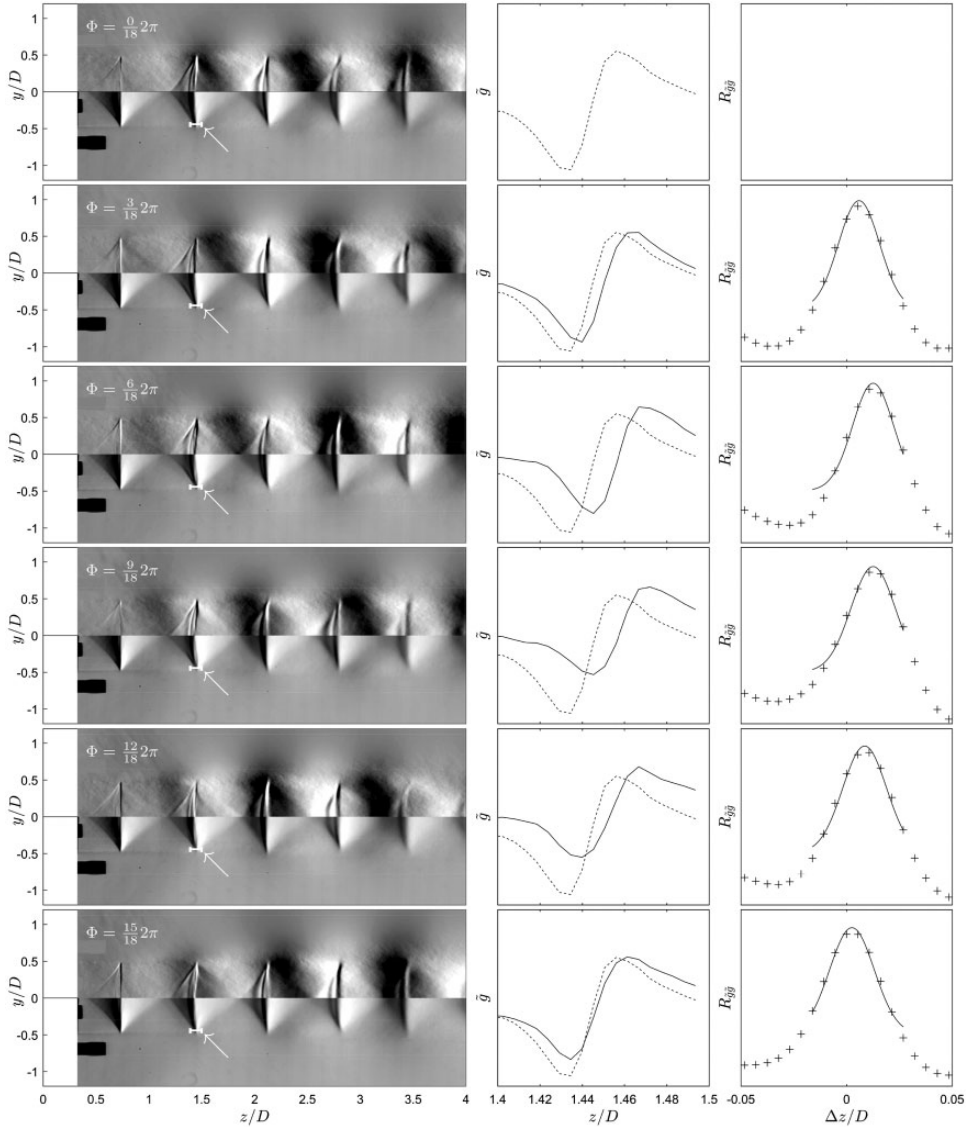


Figure 11. Left: snapshot of the phase average schlieren gray level, g^{sc} (top) and \tilde{g} (bottom), over a screech period. Center: gray level across the white line. Right: + cross-correlation function between the instantaneous and the reference gray levels, — Gaussian fit.

For each tracked shock, a probed line plotted in white in the figure is defined. According to equation (2), the gray-level profile $\tilde{g} = \bar{g} + g^{sc}$ is extracted for each value Φ_k of the phase along this line. The profile obtained for $k = 0$ is arbitrarily defined as the reference. Then, the cross-correlation function of each profile with the reference one is computed to determine the axial position of the shock Δz relative to this reference. The cross-correlation is determined with a resolution of one pixel, which is of the same order as the amplitude of the

shock motion. To increase this cross-correlation resolution, the top of the correlation function is fitted with a Gaussian curve from which the position of the maximum correlation can be obtained, as illustrated in Figure 11.

Results

The positions of the first five shocks are displayed in Figure 12 with respect to their average position over a screech period. This figure depicts the phase lag between the motion of the shocks and their amplitudes. For a quantitative analysis, a fitting sinusoidal function is computed in each case and superimposed in dashed line on the phase average results. A nearly perfect match between the actual shock motion and the sinusoidal function is observed for all shocks except the fifth shock of the $M_j = 1.10$ jet that would require to consider also the first harmonic to obtain a better agreement. At this stage, it would be interesting to conduct a complementary study for the following shocks to observe if this property also arises for the $M_j = 1.15$ jet and if it could be linked with the acoustic radiation of the screech first harmonic. Table 1 summarizes the measured amplitudes of the shock

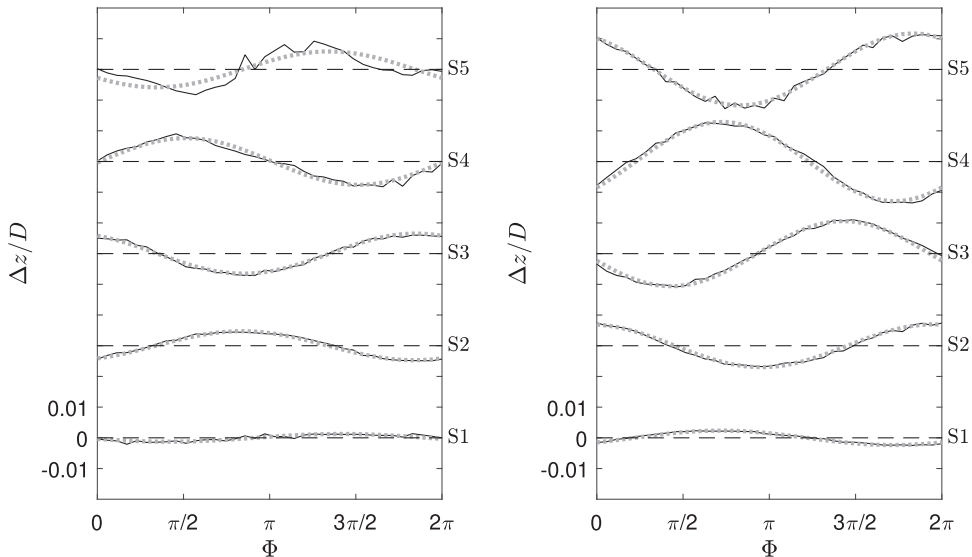


Figure 12. Position of the first five shock tips S_N during a screech period. Left: $M_j = 1.10$, right: $M_j = 1.15$. — measured position, --- sine-fitted position.

Table 1. Peak to peak amplitude of the shock motion for the first five shock cells.

M_j	$\Delta z^{pp}/D (\times 10^{-3})$				
	S1	S2	S3	S4	S5
1.10	2.5	9.5	13	15	12
1.15	4.7	14	21	26	24

motions. The motion amplitude of the first shock for $M_j = 1.15$ is found identical as the one measured by André et al.⁵¹ for the same jet, but using a different method. However, the amplitude of the second shock is found 25% lower in the present study, perhaps because of the phase averaging that smooth the shocks and reduces the contribution of the extremum events. The value obtained in the present study is also found one order of magnitude lower than those obtained by Panda⁵⁰ for the same screech mode, but neither the same Mach number nor the same experimental conditions, that turns into a screech amplitude of 149.5 dB against 144 dB measured by André et al.⁵¹ at a similar position. The amplitude of the shock motion is found to be maximum at the fourth shock for both jets. This shock location falls in the range of highest values taken by the C function plotted in Figure 10 which is consistent with the hypothesis that this region of the flow sustains the feedback loop.

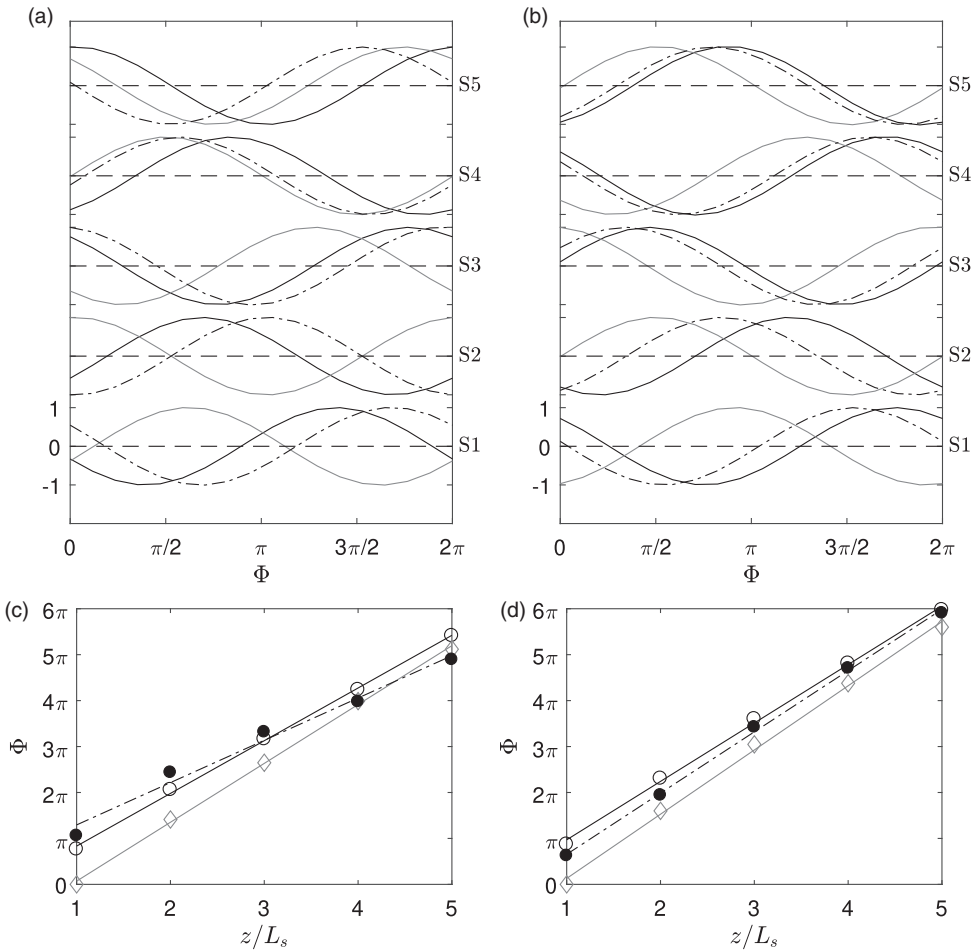


Figure 13. Left: $M_j = 1.10$ and right: $M_j = 1.15$. (a) and (b) Fitted sine of the normalized vorticity ω^{sc} in the high-speed (—) and low-speed (---) regions and the shock position (— · —) over a screech period at the first five shock tip stations. (c) and (d) Phase of the vorticity in the high-speed (○) and low-speed (◇) regions and the shock position (●) against the axial position. The straight lines are the best fitted lines.

In addition, the noisiest screeching jet also corresponds to the jet exhibiting the largest shock motion. All the present findings are in agreement with the previous study by Mercier et al.,⁴⁰ where the fourth shock has been identified as the screech source from an analysis of the near acoustic field, without excluding that other shocks may also produce lower amplitude acoustic waves.

In order to put against each other the shock motion and the vorticity field, the same procedure as for shock tracking from schlieren data has been applied to the phase-averaged axial velocity field from PIV measurements. Due to limitations in data processing, only the motion of second and third shocks has been properly captured and is used to synchronize the phase-averaged fields calculated from the PIV data with those obtained from schlieren visualizations. The evolution during a screech period of the shock position and of the vorticity along the lines of maximum vorticity defined in Figure 7(a) and (b) is superimposed in Figure 13 for each shock location. For the sake of readability, only the fitted sinusoidal functions of the phase-averaged data are presented after being normalized in amplitude. The phase of these three quantities has been extracted for each shock position, and is presented in Figure 13(c) and (d) with an arbitrary reference so that the phase of the vorticity in the low-speed region is zero at the first shock. Firstly, the phase lag between the vorticity in the high-speed and low-speed regions decreases with the axial distance as already noticed in Figure 10. Secondly, it appears clearly that in the case of the $M_j = 1.10$ jet, the phase of the shock motion is not synchronized with the vorticity. The same remark also holds for the $M_j = 1.15$ jet but with a smaller phase shift. The complexity of the shock motion, which results from the interaction between the aerodynamic field and the shock-cell pattern, but also from the acoustic field surrounding the jet that imposes unsteady boundary conditions, is well illustrated with this analysis.

Conclusion

The understanding of screech acoustic radiation is a major concern in aeroacoustics for establishing a model able to predict the screech amplitude. The shock leakage mechanism is here considered as the most probable process for describing screech radiation. Previous works have shown that shock leakage arises in mixing layers that contain a strong level of coherent vorticity, but this flow component has been little investigated in the past. In order to offer a better view of the coherent vorticity field, a phase averaging processing has been applied to the velocity fields acquired with a PIV system in the present study.

A complex structure of the spanwise vorticity field has been pointed out in mode A1 and A2 jets. It can be divided in two regions of high coherent vorticity levels that are convected at distinct phase velocities: one is located in the supersonic region of the flow and the other is located near the jet lip line in the subsonic region. The phase shift between these two regions is close to π near the nozzle and decreases further downstream. This phase shift may play an important role in the generation of the acoustic feedback of screech. The high vorticity region in the supersonic region might be responsible for shock leakage, and the vorticity near the lip line might be responsible for the upstream directivity. Those two statements lead to determine a region between the shock tip numbers 3 and 5 for $M_j = 1.10$ and numbers 2 and 4 for $M_j = 1.15$, where acoustic waves responsible for screech feedback are most likely to be emitted. A similar phase averaging is also carried out with schlieren visualizations from which the periodic motion of the shock tips is determined. For both jets, the fourth shock is found to have the largest motion amplitude. These observations together with that

obtained for the same jets in Mercier et al.⁴⁰ provide a strong confidence in stating that for the A1 and A2 modes, the shock number four has a major role in the acoustic feedback of screech.

Acknowledgments

This work was performed within the framework of the Labex CeLyA of Université de Lyon, within the program “Investissements d’Avenir” (ANR-10-LABX-0060/ANR-11-IDEX-0007) operated by the French National Research Agency (ANR).

Declaration of conflicting interests

The author(s) declared no potential conflicts of interest with respect to the research, authorship, and/or publication of this article.

Funding

The author(s) disclosed receipt of the following financial support for the research, authorship, and/or publication of this article: This work was partially supported by the industrial Chair ADOPSYS co-financed by Safran Aircraft Engines and ANR (ANR-13-CHIN-0001-01).

ORCID iD

Bertrand Mercier  <http://orcid.org/0000-0003-3468-8176>

References

1. Powell A. On edge tones and associated phenomena. *Acustica* 1953; 3: 233–243.
2. Powell A. On the mechanism of choked jet noise. *Proc Phys Soc B* 1953; 66: 1039–1056.
3. Massey KC and Ahuja KK. Screech frequency prediction in light of mode detection and convection speed measurements for heated jets. In: *3rd AIAA/CEAS Aeroacoustics Conference*, 1997, Atlanta, GA, U.S.A., AIAA paper no. 97–1625.
4. Panda J. An experimental investigation of screech noise generation. *J Fluid Mech* 1999; 378: 71–96.
5. Gao JH and Li XD. A multi-mode screech frequency prediction formula for circular supersonic jets. *J Acoust Soc Am* 2010; 127: 1251–1257.
6. Nagel RT, Denham JW and Papathanasiou AG. Supersonic jet screech tone cancellation. *AIAA J* 1983; 21: 1541–1545.
7. Norum TD. Control of jet shock associated noise by a reflector. In: *9th Aeroacoustics Conference*, 1984, Williamsburg, VA, U.S.A., AIAA paper no. 84–2279.
8. Ahuja KK. Some unique experiments on receptivity. In: *Shear Flow Control Conference*, 1985, Boulder, CO, U.S.A., AIAA paper no. 85–0533.
9. Raman G, Panda J and Zaman KBMQ. Feedback and receptivity during jet screech: influence of an upstream reflector. In: *35th Aerospace Sciences Meeting and Exhibit*, 1997, Reno, NV, U.S.A., AIAA paper no. 97–0144.
10. Harper-Bourne MJF. The noise from shock waves in supersonic jets. Noise mechanisms. In: *AGARD Proceedings*, 1974, Brussels, Belgium, paper no. CP 131.
11. Kweon YH, Tsuchida M, Miyazato Y, et al. The effect of reflector with sound-absorbing material on supersonic jet noise. *J Therm Sci* 2005; 14: 22–27.
12. Tanna H. An experimental study of jet noise part i: turbulent mixing noise. *J Sound Vib* 1977; 50: 405–428.
13. Norum TD and Seiner JM. Broadband shock noise from supersonic jets. *AIAA J* 1982; 20: 68–73.

14. Bridges JE and Wernet MP. Turbulence associated with broadband shock noise in hot jets. In: *14th AIAA/CEAS Aeroacoustics Conference*, 2008, Vancouver, Canada, AIAA paper no. 2008–2834.
15. André B, Castelain T and Bailly C. Broadband shock-associated noise in screeching and non-screeching underexpanded supersonic jets. *AIAA J* 2013; 51: 665–673.
16. Tam C, Seiner J and Yu J. Proposed relationship between broadband shock associated noise and screech tones. *J Sound Vib* 1986; 110: 309–321.
17. Tam CK. Supersonic jet noise. *Annu Rev Fluid Mech* 1995; 27: 17–43.
18. Umeda Y and Ishii R. On the sound sources of screech tones radiated from choked circular jets. *J Acoust Soc Am* 2001; 110: 1845–1858.
19. Suzuki T and Lele SK. Shock leakage through an unsteady vortex-laden mixing layer: application to jet screech. *J Fluid Mech* 2003; 490: 139–167.
20. Berland J, Bogey C and Bailly C. Numerical study of screech generation in a planar supersonic jet. *Phys Fluids* 2007; 19: 075105.
21. Shariff K and Manning TA. A ray tracing study of shock leakage in a model supersonic jet. *Phys Fluids* 2013; 25: 076103.
22. Edgington-Mitchell D, Oberleithner K, Honnery DR, et al. Coherent structure and sound production in the helical mode of a screeching axisymmetric jet. *J Fluid Mech* 2014; 748: 822–847.
23. Raman G. Supersonic jet screech: half-century from Powell to the present. *J Sound Vib* 1999; 225: 543–571.
24. André B. http://acoustique.ec-lyon.fr/jetnoise_uk.php, 2011
25. André B, Castelain T and Bailly C. Experimental study of flight effects on slightly underexpanded supersonic jets. *AIAA J* 2016; 55: 57–67.
26. Westley R and Woolley J. The near field sound pressures of a choked jet during a screech cycle. *Agard Cp* 1969; 42: 23-1–23-13.
27. Panda J and Seasholtz R. Density measurement in underexpanded supersonic jets using Rayleigh scattering. In: *36th AIAA Aerospace Sciences Meeting and Exhibit*, 1998, Reno, NV, U.S.A., paper no. 98–0281.
28. Alkisar MB, Krothapalli A and Lourenco LM. Structure of a screeching rectangular jet: a stereoscopic particle image velocimetry study. *J Fluid Mech* 2003; 489: 121–154.
29. Henderson B, Bridges J and Wernet M. An experimental study of the oscillatory flow structure of tone-producing supersonic impinging jets. *J Fluid Mech* 2005; 542: 115–137.
30. Seiner J and Norum T. Aerodynamic aspects of shock containing jet plumes. In: *6th Aeroacoustics Conference*, 1980, Hartford, CT, U.S.A., AIAA paper no. 1980–965.
31. White F. *Viscous fluid flow. McGraw-Hill International Edition*. New York, NY: McGraw-Hill Higher Education, 2006. ISBN 9780071244930.
32. Krothapalli A, Hsia Y, Baganoff D, et al. The role of screech tones in mixing of an underexpanded rectangular jet. *J Sound Vib* 1986; 106: 119–143.
33. André B, Castelain T and Bailly C. Investigation of the mixing layer of underexpanded supersonic jets by particle image velocimetry. *Int J Heat Fluid Flow* 2014; 50: 188–200.
34. Tan DJ, Soria J, Honnery D, et al. Novel method for investigating broadband velocity fluctuations in axisymmetric screeching jets. *AIAA J* 2017; 55: 2321–2334.
35. Hussain AKMF and Zaman KBMQ. The free shear layer tone phenomenon and probe interference. *J Fluid Mech* 1978; 87: 349–383.
36. Crighton DG. Acoustics as a branch of fluid mechanics. *J Fluid Mech* 1981; 106: 261–298.
37. Raman G and Rice EJ. Instability modes excited by natural screech tones in a supersonic rectangular jet. *Phys Fluids* 1994; 6: 3999–4008.
38. Panda J and Seasholtz RG. Measurement of shock structure and shock-vortex interaction in underexpanded jets using Rayleigh scattering. *Phys Fluids* 1999; 11: 3761–3777.

39. Ecker T, Brooks DR, Lowe KT, et al. Development and application of a point Doppler velocimeter featuring two-beam multiplexing for time-resolved measurements of high-speed flow. *Exp Fluids* 2014; 55: 1819.
40. Mercier B, Castelain T and Bailly C. Experimental characterisation of the screech feedback loop in underexpanded round jets. *J Fluid Mech* 2017; 824: 202–229.
41. Edgington-Mitchell DM, Weightman JL, Honnery DR and Soria J. Sound production by shock leakage in supersonic jet screech. In: *2018 AIAA/CEAS Aeroacoustics Conference*, Atlanta, GA, U.S.A., AIAA paper no. 2018–3147.
42. Westley R and Woolley J. An investigation of the near noise fields of a choked axisymmetric air jet. Technical Report, National Aeronautical Establishment (Canada) Aero, 1968.
43. Mercier B, Castelain T and Bailly C. A schlieren and nearfield acoustic based experimental investigation of screech noise sources. In: *22nd AIAA/CEAS Aeroacoustics Conference*, 2016, Lyon, France, AIAA paper no. 2016–2799.
44. Manning T and Lele S. A numerical investigation of sound generation in supersonic jet screech. In: *6th Aeroacoustics Conference and Exhibit*, 2000, Lahaina, HI, U.S.A., AIAA paper no. 2000–2081.
45. Lui C and Lele S. Sound generation mechanism of shock-associated noise. In: *9th AIAA/CEAS Aeroacoustics Conference and Exhibit*, 2003, Hilton Head, SC, U.S.A., AIAA paper no. 2003–3315.
46. Fujimatsu N and Misu I. Numerical investigation of sound generation in supersonic jet screech. In: *43rd Aerospace Sciences Meeting and Exhibit*, 2005, Reno, NV, U.S.A., AIAA paper no. 2005–796.
47. Shen H and W Tam CK. Three-dimensional numerical simulation of the jet screech phenomenon. *AIAA J* 2002; 40: 33–41.
48. Tam CK, Parrish SA and Viswanathan K. Harmonics of jet screech tones. *AIAA J* 2014; 52: 2471–2479.
49. Powell A, Umeda Y and Ishii R. Observations of the oscillation modes of choked circular jets. *J Acoust Soc Am* 1992; 92: 2823–2836.
50. Panda J. Shock oscillation in underexpanded screeching jets. *J Fluid Mech* 1998; 363: 173–198.
51. André B, Castelain T and Bailly C. Shock-tracking procedure for studying screech-induced oscillations. *AIAA J* 2011; 49: 1563–1566.

Appendix

Notation

a	Speed of sound, m/s
d	Nozzle diameter, m
f_s	Screech frequency, Hz
g	Schlieren visualization gray level
G	Gain function
L_{sc}	Shock-cell length, m
M	Mach number
NPR	Nozzle pressure ratio
p	Pressure, Pa
q	Generic quantity
Q	Level of the Q-criterion
S_N	Shock tip number N
T	Temperature, K
u	Axial velocity, m/s

U	Norm of the velocity, m/s
v	Radial velocity, m/s
y	Radial coordinate, m
z	Axial coordinate, m
γ	Heat capacity ratio
δ_θ	Momentum thickness, m
Φ	Phase with respect to a screech period, rad
ω	Vorticity component, 1/s

Superscript

\cdot^{pp}	Peak-to-peak value of a fluctuating quantity
$\bar{\cdot}$	Phase-averaged quantity
$\bar{\cdot}$	Time-averaged quantity
\cdot^{sc}	Coherent quantity, $q^{sc} = \tilde{q} - \bar{q}$
\cdot'	Fluctuating quantity, $q = \bar{q} + q'$
$\langle \cdot \rangle$	Quantity averaged by the vortex tracking procedure
\cdot^i	Quantity referring to the inner region of the mixing layer
\cdot^o	Quantity referring to the outer region of the mixing layer

Lowerscript

\cdot_i	Quantity referring to the inner region of the mixing layer
\cdot_j	Quantity referring to the equivalent ideally expanded jet
\cdot_k	Index related to the instant in the screech period
\cdot_o	Quantity referring to the outer region of the mixing layer
\cdot_{rms}	Rms value of a fluctuating quantity
\cdot_{amb}	Quantity referring to the ambient conditions